Study of strong cross-field sheared flow with the vorticity probe in the Large Plasma Device[a)]

Jean C. Perez[b)] and W. Horton[c)]
Institute for Fusion Studies, University of Texas at Austin, Austin, Texas 78712

Roger D. Bengtson[d)]
Fusion Research Center, University of Texas at Austin, Austin, Texas 78712

Troy Carter[e)]
University of California, Los Angeles, Los Angeles, California

(Received 3 November 2005; accepted 15 December 2005; published online 8 May 2006)

This work reports evidence for the existence of coherent structures in steady-state shear-flow driven plasmas in the Large Plasma Device [W. Gekelman *et al.*, Rev. Sci. Instrum. **62**, 2875 (1991)] facility at UCLA. The measurements are performed with the vorticity probe (VP), a probe that directly measures the plasma vorticity associated with the $\mathbf{E}\times\mathbf{B}$ shear flow by means of a method that is both simpler and more accurate than the methods used in neutral fluids. Because the rate of change of vorticity is a key quantity in nonlinear models, as in the Hasegawa-Mima equation, its direct measurement is critical for verification purposes. The physical origin of the rate of change of plasma vorticity from $\mathbf{E}\times\mathbf{B}$ flow is the divergence of the ion polarization current. Vortex coherent structures occur when the vorticity is a nonlinear function of the stream function. Statistical properties of vorticity are reported and shown to be consistent with the types of coherent structures created by the Kelvin-Helmholtz instability. Comparisons of the measured vortex characteristics with the results from nonlinear simulations of the systems is described. © *2006 American Institute of Physics*. [DOI: 10.1063/1.2179423]

I. INTRODUCTION

It is widely known that vorticity plays a significant role in the nonlinear dynamics of neutral fluids and plasmas. For instance, the Navier-Stokes equation has alternative formulations in terms of the fluid vorticity,[1–3] which is defined as

$$\omega \equiv \nabla \times \mathbf{v}. \tag{1}$$

The same definitions follow in fluid plasma equations, such as, magnetohydrodynamics (MHD), and generalized magnetofluid models, from which reduced sets of equations can be obtained for specific plasma conditions. The most well known of these models are the Hasegawa-Mima equation,[4] the Hasegawa-Wakatani[5] two-field equations, Hamaguchi-Horton model,[6] etc. The common feature of these models, the rate of change of vorticity, has its origin in the divergence of the plasma polarization current that provides the charge balance in the quasineutral plasma. Therefore, measuring vorticity is essential for the validation and quantitative understanding of these models. A statement of local vorticity conservation, due to the incompressibility of the $\mathbf{E}\times\mathbf{B}$ flow is

$$\frac{d}{dt}\omega = \left(\frac{\partial}{\partial t} + \mathbf{v}_E \cdot \nabla\right)\omega = S_\omega(x,t), \tag{2}$$

where the sources and sinks S_ω depend on the specific model and can act as a coupling term to other relevant dynamical fields.

Measurements of vorticity are usually obtained from fluid velocimetry, that is, vorticity is calculated by a process of finite differences on measured flow fields. One of the main disadvantages of this process is that it is prone to inherent errors in the numerical schemes used in obtaining the curl of the velocity field. In this work, we make use of the vorticity probe design, introduced in Ref. 7. This vorticity probe takes advantage of the fact that in a strongly magnetized plasma, the stream function associated with the dominant $\mathbf{E}\times\mathbf{B}$ flow is proportional to the plasma electrostatic potential as expressed by the equation

$$\mathbf{v}_E = \frac{\mathbf{E}\times\mathbf{B}}{B^2} = \frac{\mathbf{e}_z \times \nabla\varphi}{B}, \tag{3}$$

where we have taken $\mathbf{B}=B\mathbf{e}_z$. In terms of the stream function, φ/B, the magnetic-field-aligned vorticity is

$$\omega_z = \frac{1}{B}\nabla_\perp^2 \varphi. \tag{4}$$

The validity of the last equation persists as long as the turbulence is dominated by electrostatic fluctuations or magnetic fluctuations can be neglected. In this case, plasma measurements have two advantages over measurements in

[a)]Paper BI2 2, Bull. Am. Phys. Soc. **50**, 21 (2005).
[b)]Invited speaker. Electronic mail: jcperez@physics.utexas.edu
[c)]Electronic mail: horton@physics.utexas.edu
[d)]Electronic mail: bengtson@physics.utexas.edu
[e)]Electronic mail: tcarter@physics.ucla.edu

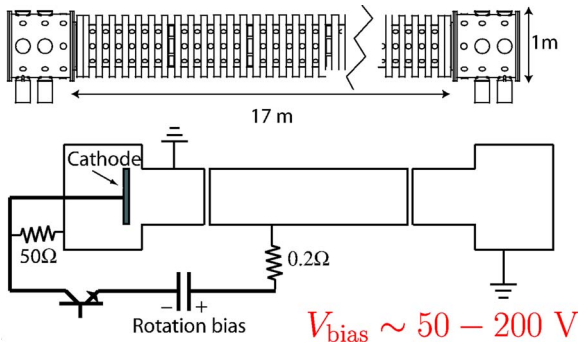

FIG. 1. Schematic of the Large Plasma Device (LAPD), including a diagram of the circuit used for plasma column biasing.

neutral fluids: (1) the stream function field can be obtained by measuring plasma potential, (2) the finite difference scheme is to be applied to a scalar rather to a vector field. Measuring vorticity under this conditions is both simpler and more accurate, provided Eq. (4) holds. The vorticity probe design and use is discussed in Ref. 7 in the context of Kelvin-Helmhotlz (KH) turbulence generated in the LArge Plasma Device (LAPD) facility at UCLA.

This paper is organized as follows. Section II is devoted to a general description of the experimental conditions in the LAPD. Section II A describes the details of the different sheared plasma rotation experiment, Sec. II B presents vorticity fluctuations measurements and statistics from the vorticity probe, and Sec. II C presents standard spectral two point correlation analysis. Section III shows a comparison of the measured wave characteristic with the linear theories available in the literature and nonlinear simulations. In Sec. IV we summarize our results.

II. EXPERIMENT ON LARGE PLASMA DEVICE

We present measurements from the vorticity probe in the upgraded LAPD[8] at the University of California, Los Angeles (UCLA). The LAPD is 18 m in length, with a plasma column ~0.8 m in diameter created by a pulsed discharge ~20 ms long from a barium oxide coated emissive cathode. The plasma parameters for these experiments were $n_e \sim 1.2 \times 10^{18}$ m^{-3}, $T_e \sim 10$ eV, and $B \sim 0.08$ T with helium as the working gas. Background neutral density at the position of the probe measurements is less than 10^{12} m^{-3} as determined by spectroscopic measurements and which is consistent with measured pressures in the LAPD. This level of neutral background gives a small ion-neutral collision frequency of order 100/s, providing a small background viscosity that is negligible for the wave numbers considered here.

TABLE I. Sheared flow regimes arising from wall biasing experiments. These regimes are classified according to the instability that is believed to drive the turbulence.

	Kelvin-Helmholtz (KH)	Drift-wave+KH
$e\tilde{\varphi}/T_e$	~1	~0.4
$\tilde{n}/n$	~0.2	~0.4
L_v	~2 cm	~5 cm
L_n	~15 cm	~5 cm
v_E	~10 km/s	~5 km/s
v_{de}	~0.6 km/s	~1.5 km/s

A. Sheared flow regimes

A sheared poloidal velocity profile is established by biasing the chamber wall with respect to the anode and cathode (see Fig. 1) for 5 ms during the discharge. This biasing results in different sheared $\mathbf{E}\times\mathbf{B}$ flow turbulent regimes at the edge of the plasma column. We classify these regimes according to the dominant instability that drives the turbulence as shown in Table I.

Figure 2(a) shows the background mean profiles for the first of these regimes, the MHD KH in which the $\mathbf{E}\times\mathbf{B}$ flow dominates the perpendicular dynamics with weak coupling to the parallel direction. In this case potential fluctuation levels are significantly higher than density fluctuations, $e\varphi/T_e \gg \delta n/n$. In Table I we see that $e\varphi/T_e=(5.0\pm0.5)\tilde{n}/n$ for the KH regime. From Table I we can also see that in the KH regime, the density scale length is about 7 times larger than the velocity scale length which allows us to ignore effects related to density gradient driven drift waves, supporting the idea of KH fluctuations dominating the turbulence. Figure 2(b) shows the second regime, a hybrid drift-wave KH in which both mechanisms are believed to drive the turbulence. Fluctuation levels for the dimensionless quantities $e\tilde{\varphi}/T_e$ and $\tilde{n}/n$ are similar up to a 10% error, characteristic of drift waves. Furthermore, the density gradient scale length of density and velocity are comparable, giving an indication that the drift wave component of the fluctuation can no longer be neglected. This regime, with a significant drift wave component[9] shows the clearest formation of the internal transport barrier[10] in the density profile consistent with the idea of suppression of turbulence and anomalous transport

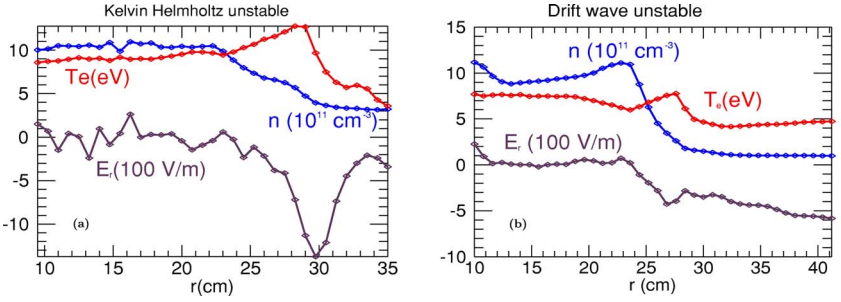

FIG. 2. Mean profiles obtained as an average in 25 experimental shots during the stationary turbulent state during the wall-bias pulse.

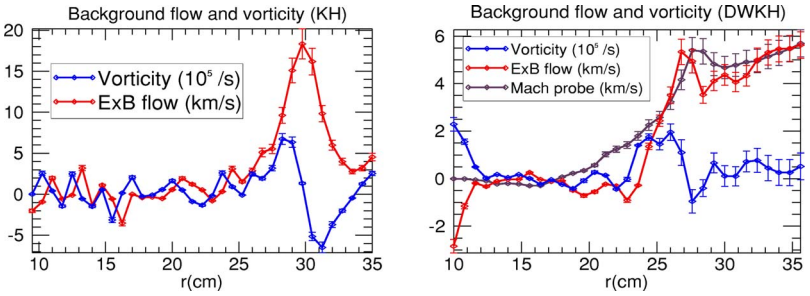

FIG. 3. $\mathbf{E}\times\mathbf{B}$ flow constructed from the average electric field during the wall bias pulse and the vorticity associated with it. Left: Kelvin-Helmholtz regime; Right: drift wave+KH regime.

by sheared flows.[11] The mode spectrum and vorticity statistic for the KH regime are reported in Ref. 7. A third regime for which there was no available data at this time is one of very weak shear with steep density gradient driven drift wave turbulence.

An early study of the KH mode in small laboratory devices include Kent *et al.*[12] with a Q machine with $L/a=100$ cm/1 cm=100, $B=0.1-0.4$ T at $T_e=0.2$ eV, and $n=5\times10^8$ to 5×10^{10} cm^{-3}. Kent *et al.* conclude that the edge oscillations over 5 kHz in frequency where $\Omega_{\max}=2\times10^4$ rad/s at the edge are KH modes and caution neglecting these modes in the stability of lower frequency drift waves. In the larger Columbia Linear Machine (CLM) Sen *et al.*[13] report the identification of KH modes at the frequency of 65 kHz. In the CLM with $L/a=100$ cm/3 cm=50, $B=0.1-0.15$ T and $Te\sim Ti\sim5$ eV, $n\sim5\times10^8$ to 5×10^9 cm^{-3}, the KH instability is a permanent feature in the region of maximum E_r which has a laboratory frequency of 55–65 kHz.

Figure 3 (left) shows the background $\mathbf{E}\times\mathbf{B}$ flow as calculated from the floating potential and temperature measurements using the triple probe for the strong shear conditions. Figure 3 (right) shows the $\mathbf{E}\times\mathbf{B}$ flow from the triple probe measurements compared to flow measurements using a Mach probe. The Mach probe used has six tantalum faces (three pairs), flush-mounted on the surface of a cylindrical probe tip. The probe is inserted so that the magnetic field is perpendicular to the axis of the cylindrical tip. Defining the angle from the direction of the magnetic field, the three face pairs are located at (0°, 180°), (45°, 225°), and (315°, 135°). The first tip pair is used to measure parallel flows, while the other two pairs are used to measure the perpendicular Mach number, as outlined in Ref. 14. The probe tips used are comparable in size to the ion gyroradius, and for this reason the computed Mach numbers are corrected for an increased effective ion collection area in unmagnetized plasmas, following Shikama *et al.*[15] A constant offset, associated with the imbalance in the area of the face pairs, has been removed from the Mach probe data by forcing the flow velocity at $r=10$ cm to be zero. The Mach probe measured flow profile is consistent with the $\mathbf{E}\times\mathbf{B}$ speed profile computed from the potential profile, although the Mach probe reports a slightly higher flow velocity. The discrepancy between the $\mathbf{E}\times\mathbf{B}$ speed and the Mach probe measurement appears largest in the density gradient region, where the difference is on the order of the diamagnetic drift velocity. These measurements put our assumptions on the perpendicular flows on firm grounds, and consequently the accuracy of the measurement of vorticity fluctuations with the vorticity probe.

B. Vorticity fluctuations

Vorticity fluctuations are obtained from the vorticity probe shown in Fig. 4. The principle behind the vorticity probe is the use of Langmuir probes in the stencil of discrete approximation of the Laplacian used in numerical computations; see, for instance, Ref. 16. The vorticity probe tips are oriented along the direction of the magnetic field (out of the page in Fig. 4). The central five tips are arranged in a diamond pattern, with the outer four tips separated from the central tip by 5 mm. The five inner tips are used to measure the floating potential, which is then used to compute a finite difference value of the vorticity. For this, four times the floating potential on the central tip must be subtracted from the floating potential on the surrounding four tips. During biased rotation experiments in the LAPD, the dc floating potential can reach values of order 200 V, substantially larger than the observed fluctuation amplitude (~1 V). The floating potential measurements are therefore performed using ac coupled amplifiers in order to reject the large low-frequency floating potential signal and to maximize the use of the dynamic range of the available digitizers.

Measurements were made using the vorticity probe at 51 radial locations. At each spatial location, data are taken from 25 different plasma discharges. The data are acquired using 14-bit, 100 MS/s digitizers. An effective sampling rate of 1.56 MS/s is obtained by averaging 64 consecutive samples

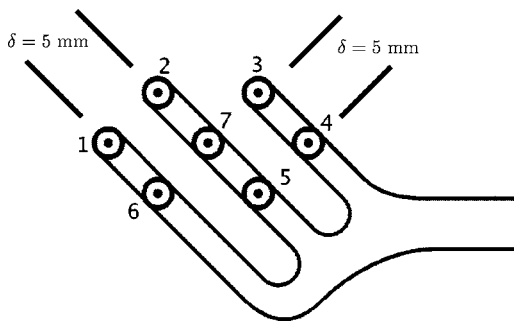

FIG. 4. Vorticity probe design. The probe is inserted into the LAPD plasma radially, so that the magnetic field is perpendicular to the surface of the probe tips and points out of the page.

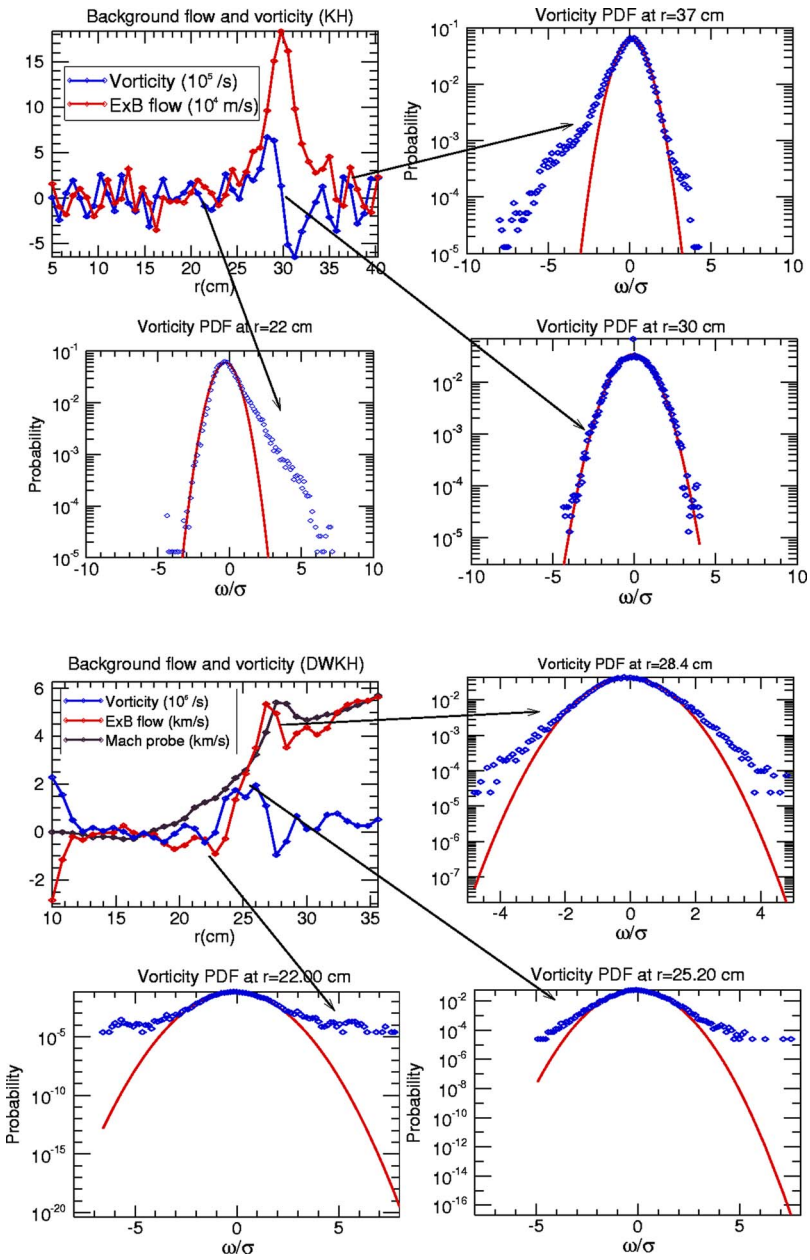

FIG. 5. Vorticity probability distribution functions for representative radius in each reported regime. PDF are constructed with vorticity fluctuation measurements from 25 experimental shots at each radius during the bias pulse, for a total of 102 400 samples.

at 100 MS/s. The averaging is done in hardware and provides an effective antialiasing filter. A total of 28 672 samples are taken during each discharge, resulting in a time record of 18.35 ms long.

Figure 5 shows probability distributions functions (PDFs) associated with vorticity at every measured radial location as compared to a Gaussian distribution represented by the solid line. The vorticity PDFs are obtained from 102 400 vorticity samples as a result of combining 25 experimental shots with 4096 time points each during the bias pulse. Vorticity PDFs show the intermittent character of vorticity through heavy tails in both regimes, which we associate with the existence of coherent structures present in the shear layer. The main qualitative difference between both regimes is the skewness of the PDFs. In the KH regime the skewness of the PDFs as one moves across the shear region presents evidence of a chain of counter rotating vortices consistent with the sign of the background vorticity. The DWKH regime does not show this antisymmetry, as we expect form the symmetric form of the background vorticity.

The skewness of the vorticity PDF in Fig. 5 with positive, counterclockwise rotating plasma vortices inside the maximum of the jet, $v_{\max} \sim 20$ km/s at $r=30$ cm shown in Fig. 2(a) and clockwise rotating vortices outside the maximum of $v_\theta(r)$ suggests the existence of patches of alternating sign vortices from the localized jet.

This configuration follows from the conservation of angular momentum and mass. Simulations in Sec. III show that like regions of vorticity with the same direction of rotation are strongly merging. Thus we may expect larger scale vortices to form in the nonlinear fluctuation spectrum.

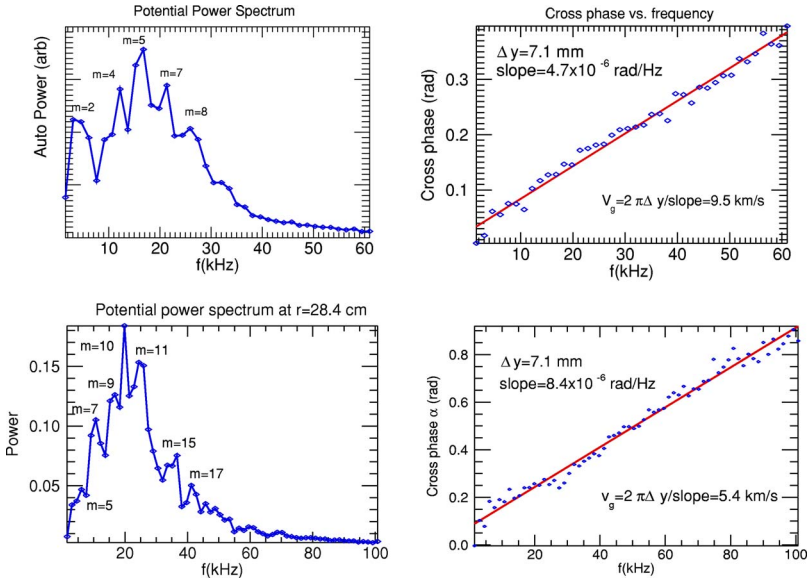

FIG. 6. Top left: Auto power spectrum for plasma potential at the center of the shear layer in the KH regime. Top right: Cross phase between two angularly separated probes for the KH regime. Bottom left: Auto power spectrum for plasma potential at the center of the shear layer in the DWKH regime. Bottom right: Cross phase between two angularly separated probes for the DWKH regime.

C. Two point spectral analysis

Using standard one and two point correlation techniques[17,18] with selected tips of the vorticity probe, wave characteristics can be obtained at different radial positions. Figure 6(a) shows the auto power spectrum for the plasma potential from the central tip 7 (see Fig. 4) at probe position $r=28.4$ cm, corresponding to the center of the shear layer. The turbulent spectrum during the bias pulse is dominated by frequencies in the range from 5 to 50 kHz. Cross phase between two angularly separated probes, shown in Fig. 6(b), can be used to identify the azimuthal mode numbers m dominant in the power spectrum.

The power spectrum is mostly localized at the shear layer region, although important levels of fluctuations are also encountered at large values of r. As the fluctuation energy appears in low mode numbers, the cylindrical geometry becomes important. The vorticity gradient term $k_y v_y''(x)$ in the Rayleigh equation (KH instability) is replaced by $(m/r)d/dr[(1/r)d/dr(r^2\Omega)]$ in the cylindrical plasma with angular rotation frequency $\Omega=v_\theta/r$. The stability analysis[19,20] shows that the centrifugal force acts as an effective gravity $g_0\mathbf{r}/a$ giving rise to the Rayleigh-Taylor instability partially controlled by the Coriolis force effect $2m\Omega$ and shear flow. In the simplest case of solid body rotation and a Gaussian density model $n(r)=n_0e^{-r^2/a^2}$ the stability is given by $A\tilde{\omega}^2+B\tilde{\omega}+C=0$, where $\tilde{\omega}$ is the Doppler shifted frequency $\omega-m\Omega$. The coefficients are $A=\nu_{m,n}(b/a)+A_p$, where b is the radius of the surrounding conducting wall and $A_p\propto k_\parallel^2$ measures the divergence of the parallel electron current, $B=2m\Omega-A_p\omega_{*e}$ from the Coriolis effect and the density gradient $\omega_{*e}=-(mT_e/eBr)(d/dr)\ln n_0(r)$ and $C=m^2(\Omega^2+g_0/a)$ the interchange instability (in a straight, axial B_z laboratory plasma $g_0=0$). The stability of the $m=1$ and $m=2$ modes depend on how close the conducting wall is to the plasma radius and the details are contained in the eigenvalue $\nu_{m,n}=m+2n+f(b/a)$, where m,n are the azimuthal and radial eigenmode numbers and $f(b/a)\to 0$ as the conducting wall moves to infinity, $b/a\to\infty$.

Examples of the eigenfunctions and eigenvalues as function of the wall-to-plasma radius and the shear in the rotation frequency $\Omega(r)$ for the modes $m=1$, 2, and 3 are shown in Ref. 19. This stability analysis suggests that the large density fluctuation observed in the edge is associated with lower m modes driven by the centrifugal force acting on the density gradient.

III. COMPARISON WITH LINEAR THEORY AND NONLINEAR SIMULATIONS

The plasma version of the KH instability can be obtained from the electrostatic response in a two-fluid model. The reduced model equation for the dynamics for the electrostatic potential is obtained from the assumption of quasineutrality,

$$\nabla\cdot\mathbf{j}=0. \tag{5}$$

Assuming the plasma to be immersed in a constant background magnetic field $\mathbf{B}=B_z\mathbf{e}_z$ we can split the current contributions into the perpendicular and parallel parts $\mathbf{j}=\mathbf{j}_\perp+\mathbf{j}_\parallel$. The perpendicular part is comprised of the currents associated with perpendicular particle and fluid drifts, namely, the polarization drift, diamagnetic drift, etc. The currents from electron and ion currents from $\mathbf{E}\times\mathbf{B}$ motion cancel each other in the quasineutral state.

Using the expression for the polarization current

$$\mathbf{j}_p=-\frac{m_in_i}{B^2}\frac{d}{dt}\nabla\varphi=-\frac{m_in_i}{B^2}\left(\frac{\partial}{\partial t}+\mathbf{v}_E\cdot\nabla\right)\nabla\varphi, \tag{6}$$

with

$$\mathbf{v}_E=\frac{\mathbf{E}\times\mathbf{B}}{B^2}=\frac{1}{B}\mathbf{e}_z\times\nabla\varphi \tag{7}$$

in (5), we obtain

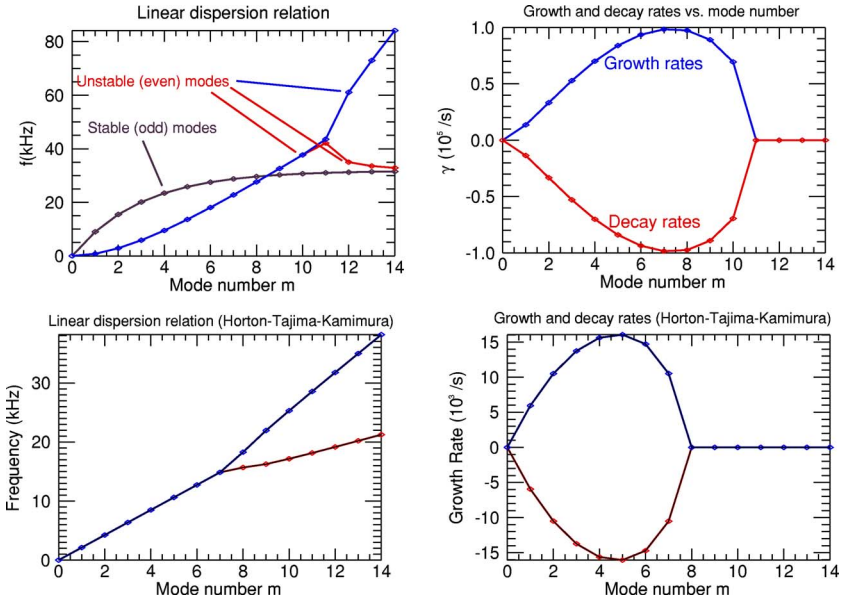

FIG. 7. Top left: Linear dispersion relation from the Rayleigh equation for a triangular jet for KH instability. Top right: Growth and decay rates for the triangular jet. Bottom left: Linear dispersion relation from Rayleigh equation for a step-up sheared flow. Bottom right: Growth and decay rates for the step-up sheared flow profile.

$$\left(\frac{\partial}{\partial t} + \mathbf{v}_E \cdot \nabla\right)\nabla^2\varphi = \frac{\partial}{\partial t}\nabla^2\varphi + [\varphi, \nabla^2\varphi] = 0, \tag{8}$$

where we have introduced the Poisson bracket between two 2D functions f, g:

$$[f,g] \equiv \frac{\partial f}{\partial x}\frac{\partial g}{\partial y} - \frac{\partial f}{\partial y}\frac{\partial g}{\partial x}. \tag{9}$$

For the KH regime, the shear layer the scale length L_{n_e}, calculated from the profile of the mean ion saturation current, gives $L_{n_e} \sim 15$ cm which is large enough to justify neglect the density gradients in the shear flow modeling. This scale length is approximately $15\rho_i$, where $\rho_i = 3$ mm.

The vorticity equation (3) is the statement that the divergence of the cross-field current vanishes. Linear dispersion

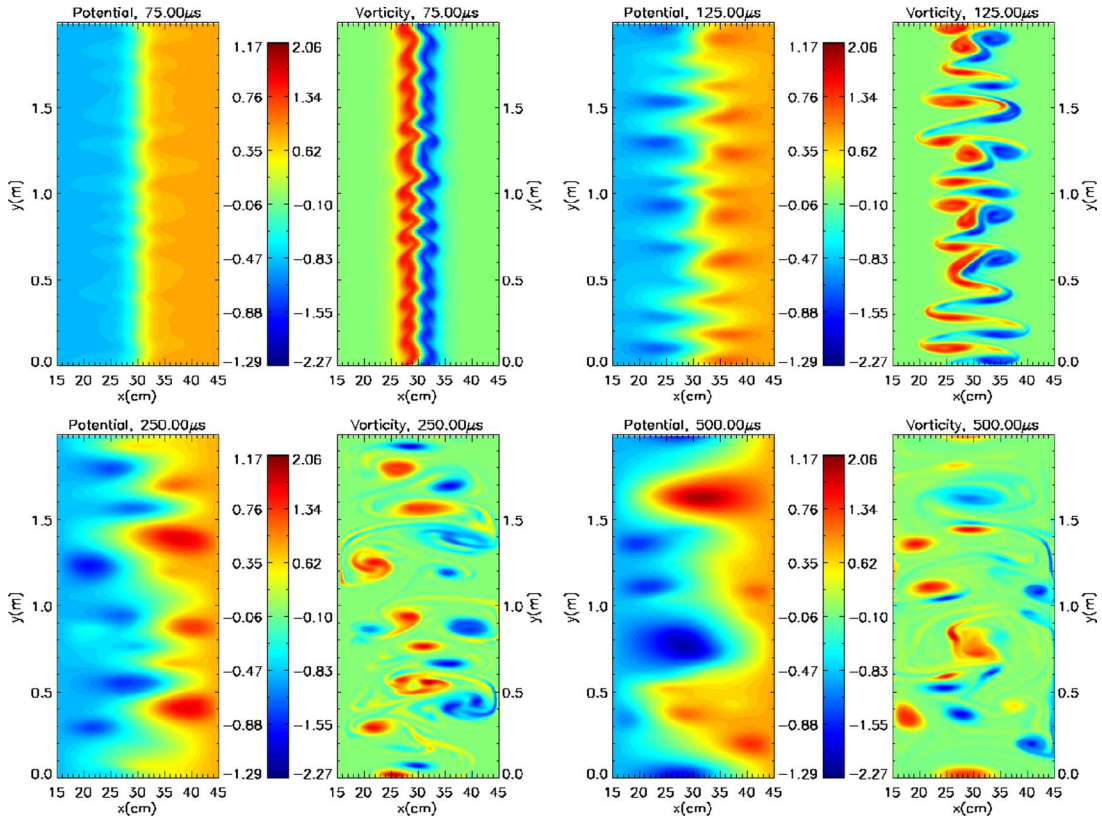

FIG. 8. Contours of potential and corresponding vorticity for selected times of nonlinear evolution.

relation for simple theoretical background profiles have been determined in Ref. 21 for the step-up flow profile in the DWKH regime and in Ref. 7 for a triangular piecewise linear jet in the KH regime. Dispersion relations are shown in Fig. 7.

Fully nonlinear simulations with similar parameters for the actual experiment are performed. The initial state is taken to be a localized jet plasma flow with some small random noise perturbation smeared out by a Gaussian filter in transform space. Contour plots of selected times in the nonlinear evolution, for electrostatic potential and its associated vorticity, are shown in Fig. 8. Initially, there are two vortex layers associated with the initial flow field in an unstable configuration. Short wavelength perturbations, $m=6,7,8,9$ grow faster in the linear stage, in accordance with the linear model, as shown in the two top frames of Fig. 8. As the instability saturates, the nonlinear term acts to generate a chain of counter rotating vortices by the self-advection of vorticity in the plasma. Merging of same sign small scale vortices gives rise to bigger vortex structures of opposite signs across the shear layer, transferring the energy to larger scales, demonstrating an inverse cascade process which explain the dominance of low mode numbers in the reported spectrum of Fig. 6.

IV. CONCLUSIONS

Measurements of ρ_s scale vorticity fluctuations were reported in the sheared rotation experiment in the Large Plasma Device facility at UCLA. Vorticity measurements show evidence for the existence of coherent structures in two different sheared flow regimes at the edge of the plasma column. In the first regime, a localized plasma jet drives the KH instability giving rise to a chain of counter rotating vortices with signs being consistent with the antisymmetric background vorticity profile. Evidence of this is shown in the heavy tails present in the vorticity probability distribution functions and the sign change of the corresponding skewness across the shear layer. In the second regime, a step-up shear profile, with weaker rotation speed, drives drift wave instability in the presence of a sheared flow. Here, the vorticity probability distribution functions still show heavy tails but with no apparent skewness.

Spectral analysis of the turbulent data showed the existence of coherent waves propagating around the axis of the machine with speeds of the order of the rotation speed. Mode numbers are determined from cross phase plots which are in good agreement with the most unstable modes previously predicted by linear theory. However, once the modes saturate and the nonlinearity takes over, an inverse cascade process from the merging of like-sign vortices will transfer the energy to the lower mode numbers, explaining the dominance by low mode numbers in the fluctuation spectrum.

ACKNOWLEDGMENTS

The authors would like to thank J. E. Maggs, R. J. Taylor, and P. Pribyl for assistance with the biased rotation experiments on the LAPD and M. Fassler for technical assistance in the construction of the vorticity probe.

The work was supported under the U.S. Department of Energy Contract No. DE-FG02-04ER 54742. Experimental work was performed at the UCLA Basic Plasma Science Facility which is funded by NSF and DOE.

[1] G. K. Batchelor, *An Introduction to Fluid Mechanics* (Cambridge University Press, Cambridge, 1967).
[2] L. D. Landau and E. M. Lifshitz, *Fluid Mechanics* (Pergamon, Oxford, 1979).
[3] S. Chandrasekar, *Hydrodynamics and Hydromagnetic Stability* (Dover, New York, 1961).
[4] A. Hasegawa and K. Mima, Phys. Fluids **21**, 87 (1978).
[5] A. Hasegawa and M. Wakatani, Phys. Rev. Lett. **50**, 682 (1983).
[6] S. Hamaguchi and W. Horton, Phys. Fluids B **4**, 319 (1992).
[7] W. Horton, J. C. Perez, T. Carter, and R. Bengston, Phys. Plasmas **12**, 022303 (2005).
[8] W. Gekelman, H. Pfister, Z. Lucky, J. Bamber, D. Leneman, and J. Maggs, Rev. Sci. Instrum. **62**, 2875 (1991).
[9] T. A. Carter, J. E. Maggs, and D. C. Pace, Europhys. Conf. Abstr. **29C**, 04.017 (2005).
[10] R. J. Taylor, M. L. Brown, and B. D. Fried, Phys. Rev. Lett. **63**, 2365 (1989).
[11] P. W. Terry, Rev. Mod. Phys. **72**, 109 (2000).
[12] G. Kent, N. Jen, and F. F. Chen, Phys. Fluids **12**, 2140 (1969).
[13] A. K. Sen, V. Reva, and K. Avinash, Phys. Plasmas **8**, 4772 (2001).
[14] J. P. Gunn, C. Boucher, P. Devynck, I. Duran, K. Dyabilin, J. Horacek, M. Hron, J. Stockel, G. V. Oost, H. V. Goubergen, and F. Zacek, Phys. Plasmas **8**, 1995 (2001).
[15] T. Shikama, S. Kado, A. Okamoto, S. Kajita, and S. Tanaka, Phys. Plasmas **12**, 044504 (2005).
[16] M. Abramowitz and I. Stegun, *Handbook of Mathematical Functions* (Dover, New York, 1970).
[17] E. J. Powers, Nucl. Fusion **14**, 749 (1974).
[18] D. E. Smith and E. J. Powers, Phys. Fluids **16**, 1373 (1973).
[19] J. Liu, W. Horton, and J. E. Sedlak, Phys. Fluids **30**, 467 (1987).
[20] W. Horton and J. Liu, Phys. Fluids **27**, 2067 (1984).
[21] W. Horton, T. Tajima, and T. Kamimura, Phys. Fluids **30**, 3485 (1987).